ORIGINAL PAPER

Stress transmission in systems of faceted particles in a silo: the roles of filling rate and particle aspect ratio

M. Acevedo · I. Zuriguel · D. Maza · I. Pagonabarraga · F. Alonso-Marroquin · R. C. Hidalgo

Abstract We present experimental and numerical results for particle alignment and stress distribution in packings of faceted particles deposited in a small-scale bi-dimensional silo. First, we experimentally characterize the deposits' morphology in terms of the particles' aspect ratio and feeding rate. Then we use the experimental results to validate our discrete element method (DEM) based on spheropolygons. After achieving excellent agreement, we use contact forces and fabric provided by the simulations to calculate the coarse-grained stress tensor. For low feeding rates, square particles display a strong tendency to align downwards, i.e., with a diagonal parallel to gravity. This morphology leads to stress transmission towards the walls, implying a quick development of pressure saturation, in agreement with the Janssen effect. When the feed rate is increased, both the disorder and the number of horizontal squares in the silo increase, hindering the Janssen effect. Conversely, for elongated particles the feed rate has a weak effect on the final deposit properties. Indeed, we always observe highly ordered structures of horizontal rods where the stress is transmitted mainly in the vertical direction.

M. Acevedo · I. Zuriguel · D. Maza · R. C. Hidalgo (✉)
Departamento de Física, Facultad de Ciencias, Universidad de Navarra, 31080 Pamplona, Spain
e-mail: raulcruz@unav.es

I. Zuriguel
e-mail: iker@unav.es

I. Pagonabarraga
Departament de Física Fonamental, Carrer Martí i Franqués 1, Universitat de Barcelona, 08028 Barcelona, Spain

F. Alonso-Marroquin
School of Civil Engineering, The University of Sydney, Sydney, NSW 2006, Australia

1 Introduction

In the last decade there has been an increasing interest in exploring how particle shape affects stress transmission in two classical granular systems: sandpiles [1–5] and silos. For this latter case, previous works have paid attention to both charge [6,7] and discharge processes [8–11]. Moreover, some authors have attempted to investigate the special behavior of particles with flat faces, which are widely found in geomaterials and food processing, and their understanding becomes a major issue for handling of raw materials. For instance, it is known that polyhedral particles reduce flowability because they increase the material shear strength [12–15], a factor of vital importance to civil-engineering applications [16].

Previous efforts at capturing particle shape in DEM have been focused on including rolling friction and torsion between the particles [17–19]. Other authors have chosen to reproduce the real particle shape as closely as possible. Particle shapes have been identified directly from digitized images [21], represented either by superquadrics [22], polygons or polyhedra [6,7,23–29], spheropolygons or spheropolyhedra [30–33] or by clumps of disks or spheres [8,9,19]. Moreover, advanced models that included contact geometry and particle geometry have been developed by combining DEM with finite element formulations [34–36].

In granulate systems, macroscopic fields (density and momentum) can be extracted from the local properties of the interacting particles using averaging strategies and coarse-grained formulations [37–43]. These approaches allow a constitutive description of the granular media, which usually feature as a compressible complex fluid [44]. Within these

micro-macro formulations, the load transmission in granular systems has been examined by using the fabric and stress tensors, which have been defined for both dynamic and quasi-static systems [37–43]. This framework has been exploited to find correlations between the packing morphology and the stress transmissions in the granular media [6,7,12].

An intriguing characteristic of particulate materials in a static configuration is that they are history-dependent. This implies that one should consider the building mechanism from which the grain assembly has been attained. For the case of piles, it has been shown that the dip size at its base may be strongly modified and even disappear depending on the pouring protocol [45,46]. It is also well known that the silo filling method importantly affects wall stress transmission [47–50].

In this paper, we investigate the effect that the silo feeding rate has on stress transmission between faceted particles. The filling rate is controlled by fixing the mean velocity of the particles as they are fed in while changing the volume fraction of the granular material. We examine three cases, each with particles of a different aspect ratio, to find the importance of particle shape for understanding the properties developed in a static granular sample. Finally, the comparison of experimental and numerical results allows the discovery of non-trivial rearrangements of the particles, and unexpected pressure profiles, which could be relevant when handling faceted particles in real silos.

2 Experimental procedure

A two-dimensional silo was filled at different feeding rates with grains of different shape. The experimental setup is a variation of the one originally described in Ref. [48,49]. The system has two compartments, both of width $W = 258$ mm: a top reservoir of height 750 mm (**B** in Fig. 1), and a silo below of height 750 mm (**D** in Fig. 1) into which the particles are deposited. The whole system is built with four glass plates 6 mm: two for the reservoir (front and rear), and two for the silo (see Fig. 1). The two lateral walls are stainless steel strips 1650 mm high and 3.3 mm thick, keeping the front and rear glass plates at a distance larger than the thickness of the particles (3 or 3.16 mm) to confine them with freedom to move in a mono-layer. Between the two compartments, a removable flat metal piece of length 258 mm and width 1 mm keeps the particles from falling into the silo when they are initially poured into the top reservoir. The flat bottom of the silo is formed by two metal pieces that are drawn apart to allow discharge of the particles from the silo, after every experimental realization.

At the bottom of the **B** reservoir, (indicated with **C** in Fig. 1) a series of obstacles (1 mm length) are uniformly placed to control the feeding rate: increasing the obstacle den-
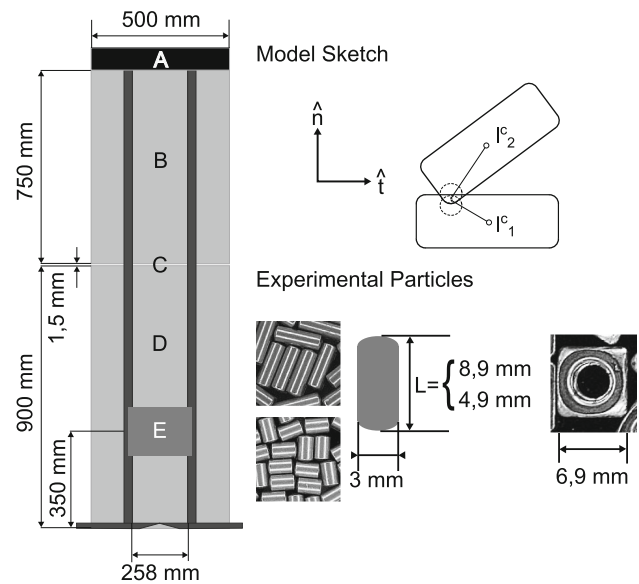

Fig. 1 *Left* experimental setup showing the *top* reservoir, the silo, and dimensions of the compartments. The label *E* marks the region at which the deposits were recorded. At *top right* is a sketch of the particles' interaction model. (see text for details) At the *bottom-right* is the scheme of the experimental particles used in this work

sity reduces the mean feeding rate. For each particle shape, three or four obstacle configurations are used to obtain different feeding rates. Moreover, a measurement was taken in an additional configuration also: pouring the grains in at the top of the system with neither the obstacles nor the removable metal piece between the two compartments in place. Provided that this pouring was quite slow, we could obtain the smallest feeding rate that is comparable with previous results reported in Ref. [6].

The experimental procedure to generate the deposits is as follows. First the top reservoir *B* is filled homogeneously along its whole width through a hopper from above (**A** in Fig. 1). When all the particles are deposited, the metal piece that was previously placed at the bottom of the *B* reservoir is removed, and the grains fall into the silo under gravity. Images of the deposit are recorded in a region that covers the whole width of the silo and a height that goes from 290 mm to 410 mm from the bottom of the silo (the region marked with *E* in Fig. 1). This region was chosen to ensure that any possible local effect of the bottom boundary is negligible, a fact that was proven in Ref. [6]. The images are processed to obtain the centres and orientations of the particles. We have shown earlier that the vertical (lateral) walls induce local particle alignment [10,51]. The contribution of this local alignment is removed by discarding particles whose centre of mass is closer than 40 mm to the lateral walls. Once the deposit is recorded, the outlet at the bottom of the silo is opened until it is completely emptied. One hundred realizations were performed for each feeding rate and particle type, to achieve good statistics.
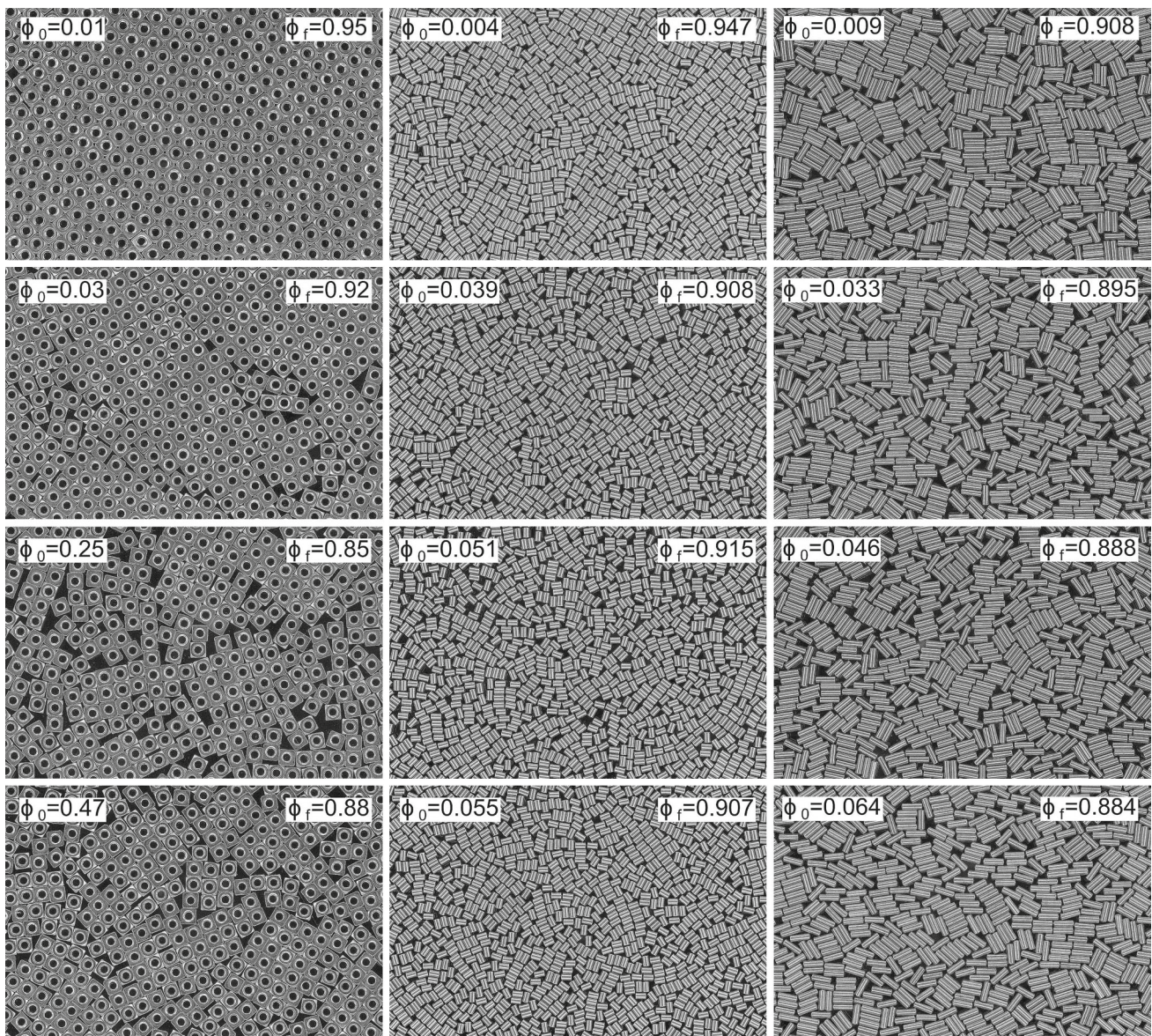
Fig. 2 Photographs of the deposits (region E in Fig. 1) obtained for particles with three different aspect ratios: *left column d = 1, central column d = 5/3*, and *right column d = 3*. In each case, experimental deposits are presented for several initial volume fractions (ϕ_0), and its correspondig final packing fraction (ϕ_f) as indicated in legends

The square particles were DIN 557 M4 nuts with $D = 6.9$ side and 3.16 mm thickness. The other two types were monodisperse cylindrical stainless steel rods (diameter $D = 3$ mm), of lengths $L_S = 4.9$ mm and $L_L = 8.9$ mm. Hence the aspect ratios of particles were $d = D/D = 1$, $d = L_S/D = 1.63$ ($d \approx 5/3$), and $d = L_L/D = 2.97$ ($d \approx 3$). About 8.0×10^3 rods of $d \approx 3$ were used, and about 1.4×10^4 of $d \approx 5/3$. About 5×10^3 square particles were used. Some examples of packings obtained for different feeding rates (initial volume fractions) are shown in Fig. 2.

With the purpose of estimating the feeding rates as accurately as possible, we performed all the measurements during each experimental realization in the same section of the silo where the deposits are analyzed. The feeding rates were measured using a high-speed camera at 3000 frames per second that registered a region of height 330 to 370 mm, (region marked with **E** in Fig. 1) and across the whole width of the silo. The recordings were performed during one second when the front of accumulating particles, where deposits were being formed, was still below the recording region. For each experimental condition, we calculated the average feeding rate for five different depositions. Note that the feeding rate f (measured as number of particles per second) depends on the mean volume fraction, ϕ_0, and the mean particle velocity, v, at the recording region: $f = v\phi_0 W/A$; where W is the width of the silo and A the area of a single particle. As the

particles are all poured from the same position, their velocity in the region described above is measured to be constant at 350 ± 10 cm/s. Hence, in our experiments the placement of the obstacles affects the feeding rate by modifying the initial volume fraction, ϕ_0, at the region of measurement. Therefore, ϕ_0 will be used as the control parameter. It is important to remark, that the control parameter ϕ_0 should not be confused with the final packing fraction of the deposit ϕ_f. The correlation between ϕ_0 and ϕ_f have been carefully examined in previous works [48,49].

Variation of the feeding rate by modifying ϕ_0, while keeping constant the velocities of the particles (at a given height), corresponds to the usual situation in real silos where grains are deposited from a given height at zero initial velocity. Alternative experiments where the feeding rate is varied at constant ϕ_0 are of great interest but outside the scope of this work. Let us note that the effect of higher velocities on the morphology of deposits is negligible for low values of ϕ_0. We have established this by comparing our findings with results from other studies, where the silos are filled from lower positions and differences are not recognized [7].

3 DEM simulations

The numerical method used in this paper is based on the Minkowski sum approach introduced for DEM simulations [30–32]. For our bidimensional model we adopt the concept of spheropolygons [31] that has been implemented in the in-house software SPOLY. This software consists of a simulator that is written in C++ following the object-oriented-design philosophy, and a Visual Basic graphical interface for pre- and post-processing and rapid construction of models. The simulator uses an explicit numerical scheme that solves the translational and rotational particles' equations of motion in two dimensions [32]. To achieve high-performance simulations, the code uses dynamic allocation of memory, and a combination of the linked cells and Verlet lists that reduces the amount of calculation of contact forces between the spheropolygons [32].

A 2D granular system of spheropolygons with four vertices was numerically implemented (see Fig. 1). We use smoothed rectangles with aspect ratio d, defined as the ratio between particle length and width. The system is confined within a rectangular box of width $W = 256$ mm and with lateral and bottom boundaries built of fixed particles. Particles are continuously added at a volume fraction ϕ_0 at the top of the box, with a prescribed feeding rate and random orientation. This is achieved by choosing an initial particle velocity parallel to gravity with a magnitude close to the mean value observed experimentally. Particles settle due to gravity, and relax until their mean kinetic energy is several orders of magnitude smaller than their elastic potential energy. We

have simulated 3×10^4 squares with side 6.9 mm ($d = 1$), 9×10^3 rods of $d = 5/3$, and 5×10^3 rods of $d = 3$. For both rods the shorter side is 3 mm. To get good statistics, results are obtained averaging over at least eight different realizations for each case.

The contacting force between a pair of particles, i and j, is determined by the repulsive force, $\mathbf{F}_{ij}$, they exert on each other. This force can be decomposed as $\mathbf{F}_{ij} = F^N \hat{\mathbf{n}} + F^T \hat{\mathbf{t}}$, where F^N is the magnitude of the force along the normal direction $\hat{\mathbf{n}}$ to the contact plane that characterizes the overlap between the two particles, and F^T is the magnitude of the force acting along the direction parallel to the contact plane, identified by the unit vector $\hat{\mathbf{t}}$. The normal interaction, F^N, has a conservative and a dissipative contribution. The former is expressed as an elastic force, proportional to the overlap distance δ. The latter corresponds to a velocity-dependent viscous force. Hence, the total normal force reads $F^N = -k^N \delta - \gamma^N m_r v_{rel}^N$, where k^N is the spring constant in the normal direction, $m_r = m_i m_j / (m_i + m_j) = m/2$ stands for the pair's reduced mass, γ^N is the damping coefficient, and v_{rel}^N is the normal relative velocity between the pair of particles. The tangential force F^T also contains an elastic term and a tangential frictional term accounting for static friction between the grains. We take into account Coulomb's friction which reads $F^T = \min\{-k^T \xi - \gamma^T m_r \cdot |v_{rel}^T|, \ \mu F^N\}$, where γ^T is the damping coefficient in tangential direction, and v_{rel}^T is the tangential component of the relative contact velocity of the overlapping pair. ξ represents the elastic elongation with spring constant k^T at contact, which increases as $d\xi(t)/dt = v_{rel}^T$ as long as there is an overlap between the particle pair, while μ is the corresponding friction coefficient.

The values for normal and tangential elastic constants are $\frac{k^T}{k^N} = 0.1$ and $k^N = 10^4$ N/m. The ratio between normal and tangential damping coefficients is taken as $\frac{\gamma^N}{\gamma^T} = 3$, while gravity is set to $g = 10$ m/s^2 and the time step to $\Delta t = 10^{-6}$ s. We have ensured that the kinetic energy loss and the dynamics of sediment formation are analogous to those observed experimentally. We have converged to $\gamma^T = 10^2$ s^{-1} and $\mu = 0.4$ as the best parameters to fit the coefficient of restitution and sliding resistance between two faceted particles. In all the simulations reported here we have kept constant the previous set of parameters modifying only the volume fraction of the initial configuration, ϕ_0.

4 Results

4.1 Packing morphology

Let us start by describing the experimental photographs displayed in Fig. 2. For square particles, $d = 1$, the smallest initial volume fraction, $\phi_0 = 0.01$, leads to an almost per-
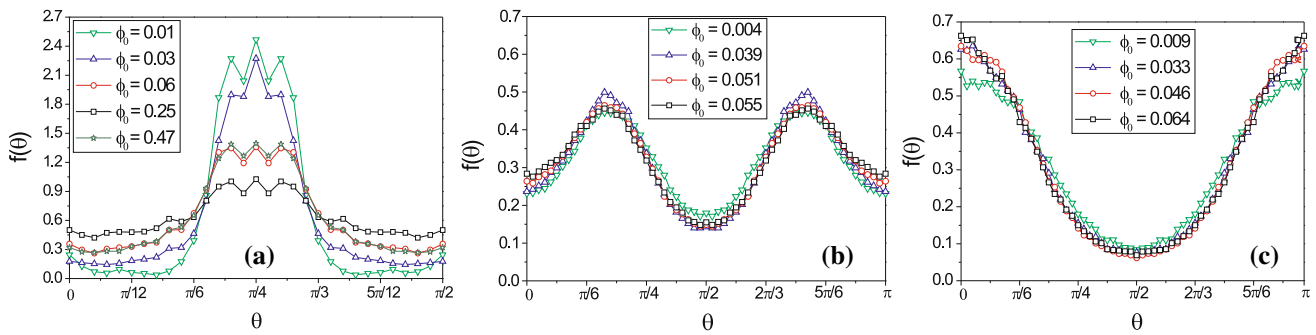
Fig. 3 Orientation distributions for particles with three different aspect ratios: **a** $d = 1$, **b** $d = 5/3$, and **c** $d = 3$. In each case, experimental results are presented for several initial volume fractions as indicated in legends

fectly ordered configuration. Interestingly, in these deposits all the particles align pointing downwards (i.e., with their diagonal parallel to gravity). When the initial volume fraction is increased to $\phi_0 = 0.03$, the order decreases as some defects start to develop in the deposit. At larger initial volume fractions, for $\phi_0 = 0.25$, there is clear reduction in both the particle order and the tendency of the squares to align with their diagonal parallel to gravity. Finally, a further increase of ϕ_0 does not reveal a significant effect in the structure and order of the deposits. For short rods, $d = 5/3$, a similar trend is observed concerning the ordering: increasing the initial volume fraction leads to a reduction of order in the structure. Yet the disorder achieved in the deposits of rods of $d = 5/3$ is smaller than for squares. Longer rods, $d = 3$, display once more the same behavior and a significant fraction of rods oriented horizontally.

The particle-orientation distribution function, $f(\theta)$, expressed in terms of the angle θ that the particle's long axis makes with the horizontal (or a side for square particles), is shown in Fig. 3. Due to symmetry, the angle satisfies $0 < \theta < \pi$ for rods and $0 < \theta < \pi/2$ for squares. As suggested by the photographs shown in Fig. 2, squares strongly align with their diagonal parallel to gravity, $\theta = \pi/4$, especially for the smallest feeding rate. This is evident from the distributions shown in Fig. 3a, where a marked peak is always observed at $\theta = \pi/4$. Increasing ϕ_0 leads to a reduction of the peak, although for the highest ϕ_0 the number of particles oriented at $\theta = \pi/4$ increases again. Conversely, the number of squares aligned horizontally ($\theta = 0$ or $\theta = \pi/2$) increases with ϕ_0. Again, for $\phi_0 = 0.47$ the tendency is reversed and a reduction of the number of particles oriented at $\theta = 0$ or $\theta = \pi/2$ is observed.

The outcomes for elongated particles are markedly different. Fig. 3b shows that the preferred orientation of rods with $d = 5/3$ is around $2\pi/11$, independently of the initial volume fraction. Interestingly, rods aligned vertically ($\theta = \pi/2$) correspond always to the least probable orientation. Furthermore, another minimum in $f(\theta)$ is found for rods aligned horizontally ($\theta = 0$ or $\theta = \pi$). Elongated particles are less

sensitive to the filling method; only a small effect is found in the number of horizontal particles seems to increase with ϕ_0. Finally, Fig. 3c shows that $d = 3$ rods have a marked preference to align horizontally; that is, perpendicular to gravity. Again, the minimum in the distribution is found for the vertical orientation. As in previous cases, increasing ϕ_0 leads to a slight increase in the fraction of horizontally aligned particles.

We quantify the morphology of the deposits and the degree of local ordering by means of the radial distribution function, which can be expressed as:

$$g(r) = \left\langle \frac{N(r + \delta r)}{\rho 2\pi r \delta r} \right\rangle \quad (1)$$

where $\rho = N_T/S$ is the average number of particles per unit of area and is measured by counting the total number of particles, N_T, whose of mass lies in the analysed area, S. $N(r + \delta r)$ accounts for the number of particles with its centre of mass at a distance r, measured in units of the rod diameter D (or square side), within a differential of area $\delta S = 2\pi r \delta r$, where we choose $\delta r = 0.1$. Note that for very dense system of perfectly aligned particles, the value of this parameter controls the height of the peaks of $g(r)$. In order to avoid finite size effects, we have performed our analysis only for those particles a distance $4r$ away from the border of the analysed region; accordingly, we obtain results reliable for $r < 4$.

Figure 4 displays the $g(r)$ for all the particle shapes and feeding rates analyzed in this work. Fig. 4a shows that square particles display marked peaks for $r = 1, 2, 3, 4, \ldots$, denoting the high degree of order in the deposits. Surprisingly, a peak at $r = \sqrt{2} \approx 1.41$ is not observed in any of the distributions. This indicates that, despite the high degree of order within the sample, a perfect alignment where four particles contact each other through their corners (as schematized in the top structure of Fig. 5a) does not develop. This fact can be corroborated by visual inspection of the deposit of squares poured at $\phi_0 = 0.01$ (top left picture in Fig. 2). Effectively, the squares align face to face, but this order seems to be prop-
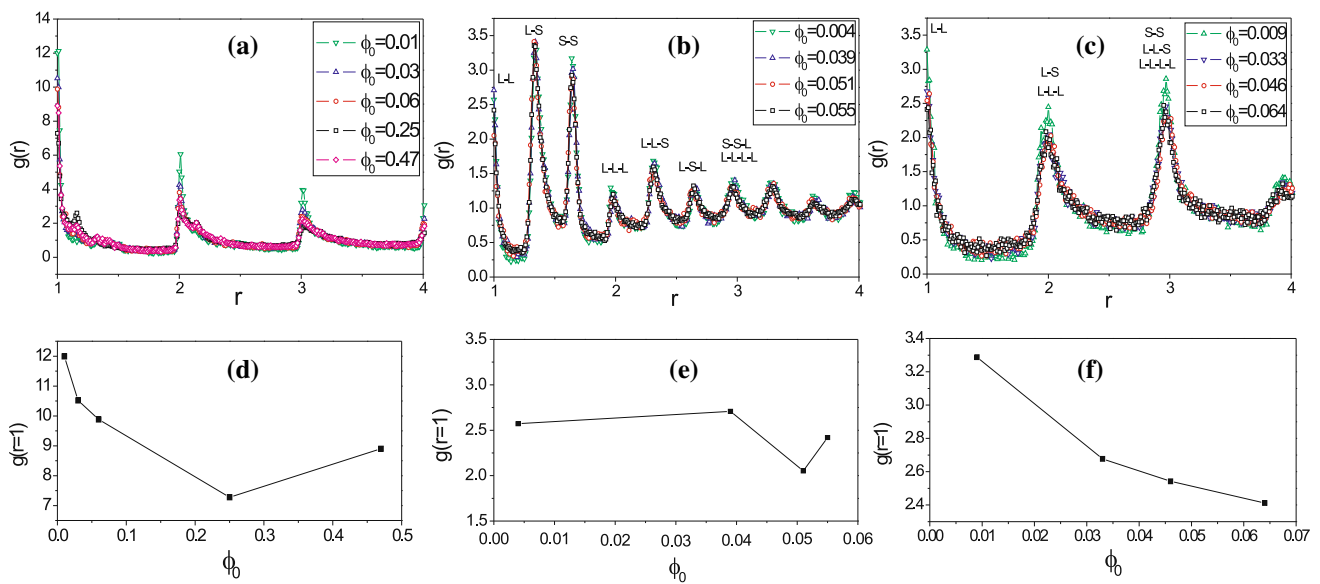
Fig. 4 Top: $g(r)$ for deposits obtained with particles of three different aspect ratios: **a** $d = 1$, **b** $d = 5/3$, and **c** $d = 3$. In each case, experimental results are presented for several initial volume fractions as indicated in legends. Bottom: $g(r = 1)$ for different values of the initial volume fraction: for **d** $d = 1$, **e** $d = 5/3$, and **f** $d = 3$ particles
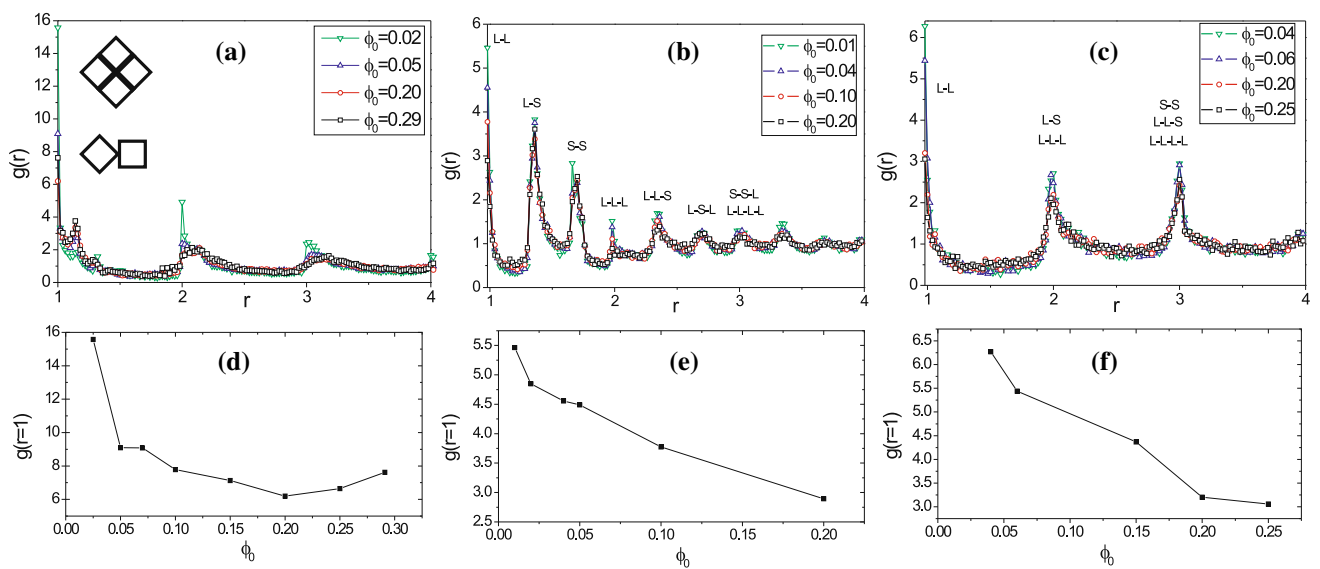

Fig. 5 Top: $g(r)$ for deposits obtained numerically with particles of three different aspect ratios: **a** $d = 1$, **b** $d = 5/3$, and **c** $d = 3$. In each case, numerical results are presented for several initial volume fractions as indicated in legends. In the insert of Figure **a** two structures of squares are schematized. The one at the top, where squares are aligned through their corners, is not observed within the deposits. The one at the bottom, where squares align face-vertex, is observed for high values of ϕ_0. Bottom: $g(r = 1)$ for different values of the initial volume fraction: for **d** $d = 1$, **e** $d = 5/3$, and **f** $d = 3$ particles

agated in rows at $\pi/4$ radians, either to the left or to the right. The squares belonging to different rows are not perfectly aligned, having their vertices separated. From Fig. 4a it is also revealed that the height of the peaks at $r = 1, 2, 3, 4, \ldots$ slightly decreases as ϕ_0 increases, indicating that the order within the sample is reduced on increasing the feeding rate. In order to explore this behavior further, Fig. 4d shows the

magnitude of the peaks for $r = 1$ ($g(r = 1)$) as a function of the initial volume fraction. As expected, $g(r = 1)$ decreases with ϕ_0 except for the case of the highest value of ϕ_0 where the tendency is reversed and $g(r = 1)$ increases again. Another indicator of the disorder developed within the deposit when the feeding rate increases is the emergence in Fig. 4a of a small peak around $r \approx 1.18$ for the two high-

est values of ϕ_0. This peak is associated with a configuration where two squares contact face-vertex (as schematized by the bottom structure in Fig. 5a) and their separation is, indeed, $r \approx 1.207$.

Figure 4b shows a richer structural behavior for $d = 5/3$ rods; the number of peaks of $g(r)$ is not restricted to integer values of r. Besides the peaks at integer values, $r = 1, 2, 3, 4, \ldots$ (which correspond to rods aligned along their long faces), new peaks are visible. The most obvious ones are at $r = 1.31$, which corresponds to a long face L, aligned with a short face S, L-S; and at $r = 1.63$, which corresponds to two rods aligned along their short faces, S–S. Small peaks are also appreciable at $r = 2.31$ and $r = 2.62$, corresponding to faces aligned in combinations L-L-S ($r = 1 + 1.31$) and L–S–L ($r = 1.31 + 1.31$) respectively. The peaks observed at larger separations can correspond to more than one combination of alignments. For example, the peak appearing at $r \approx 3$ represents S–S–L ($r = 1.63 + 1.31 = 2.94$) and L–L–L–L alignments ($r = 3$). Finally let us to note that for $d = 5/3$ rods, the feeding rate has a minor impact on the ordering observed, as depicted in Fig. 4e, which indicates that $g(r = 1)$ varies weakly with ϕ_0 and does not follow any particular trend.

Figure 4c shows that the $g(r)$ for $d = 3$ rods only displays peaks at $r = 1, 2, 3, 4, \ldots$. This is an expected result because for this particular aspect ratio, the distance corresponding to a L–S alignment is $r = 2$ and coincides with the distance for an L–L–L configuration. The same happens for $r = 3$ which is the distance resulting for S–S, L–L–S, and L–L–L–L configurations. Hence, the heights of the peaks cannot be straightforwardly related with the number of particles in a given configuration. Indeed, the fact that the peak at $r = 3$ is systematically higher than the one at $r = 2$ is due to the fact that the number of different conformations that can be formed at $r = 3$ is larger than for $r = 2$. The dependence of $g(r = 1)$ on ϕ_0 displayed in Fig. 4f indicates that for these elongated rods, the feeding rate has an effect analogous to that observed for square particles: increasing the feeding rate leads to a reduction of the order within the sample.

To validate our DEM simulations with the experimental results, the values of $g(r)$ obtained numerically are depicted in Fig. 5. Clearly, the numerical outcomes reproduce the experimental ones very accurately. Fig. 5a–c show that the peaks of $g(r)$ for the three different aspect ratios analyzed appear exactly at the same positions as in experiments. In particular, the dependence of $g(r = 1)$ on the initial volume fraction reveals strong analogies with the experiments. For square particles, $g(r = 1)$ decreases with ϕ_0 up to $\phi_0 \approx 0.2$, where the tendency is reversed and the order within the sample starts increasing. Simulations allow us to reproduce more feeding rates than experimentally, providing stronger evidence for the non-monotonic dependence of the local ordering on ϕ_0. The monotonic dependence of $g(r = 1)$ on ϕ_0 for

rods is also reproduced for the two aspect ratios considered. However, we expect a further increase of $g(r) = 1$ as ϕ_0 further increases, based on recent experimental work. Indeed, there has been found a non-monotonic behavior of the final packing fraction (which is another indicator of order within the deposit) in deposits obtained when pouring the particles from different initial volume fractions [52] or tapping the samples at different intensities [53,54]. Unfortunately, our numerical method does not allow us to achieve larger values of ϕ_0 without introducing a predefined order in the initial configuration of rods.

4.2 Packing micro-mechanics

We can further take advantage of the information provided by the DEM model and calculate the mean stress tensor within the granular column, from which we can subsequently derive the pressure profiles. Goldhirsch [41] has introduced a very elaborate definition of the mean stress field $\bar{\sigma}_{\alpha\beta}(\mathbf{r})$ at position $\mathbf{r}$ which reads

$$\bar{\sigma}_{\alpha\beta}(\mathbf{r}) = -\frac{1}{2} \sum_{i,j;i \neq j} f_{ij\alpha} r_{ij\beta} \int_0^1 ds\, \Phi[\mathbf{r} - \mathbf{r}_i + s\mathbf{r}_{ij}], \qquad (2)$$

where the sum runs over all the overlapping particle pairs i, j, whose centres of mass are at $\mathbf{r}_i$ and $\mathbf{r}_j$ respectively. The vector $\mathbf{f}_{ij}$ accounts for the force exerted by particle j on particle i, and $\mathbf{r}_{ij} \equiv \mathbf{r}_i - \mathbf{r}_j$. The coarse-grained ($CG$) function, $\Phi(\mathbf{R})$, is positive a semidefinite normalized function, with a single maximum at $\mathbf{R} = 0$. In our case, we have used a Gaussian coarse function, $\Phi(\mathbf{r}) = \frac{1}{\pi\omega^2} e^{-(r/\omega)^2}$, where the sign convention is that compressive stress is negative. The value of ω defines the coarse-grained scale.

For assessment of the impact of CG scale on the measured pressure profiles, Fig. 6 displays the trace of the stress tensor as a function of the silo depth h, normalized with the deposit width W, for various values of ω for squares and rods. The trace is derived from the stress tensor components computed within specific areas where the contact contribution within the selected area is weighted by the function $\Phi(r)$. The pressure profiles were calculated fixing the horizontal coordinate at the center of the silo, and varying the vertical one (up–down). The results reveal that stress fluctuations at fixed depth vanish when increasing the value of ω. This indicates the existence of a CG scale for which the stress tensor field is independent of resolution. In our case, however, the stress profiles are not homogeneous, due to the action of the gravity field. Consequently, one must carefully choose a value of ω small enough to accurately describe the spatial dependence of the stress field. We have also found that the particle's shape slightly affects the specific value of the CG scale ω. For squares, we have estimated $\omega = 4d$ as the optimal value, while for rods with $d = 5/3$ (data not shown) and
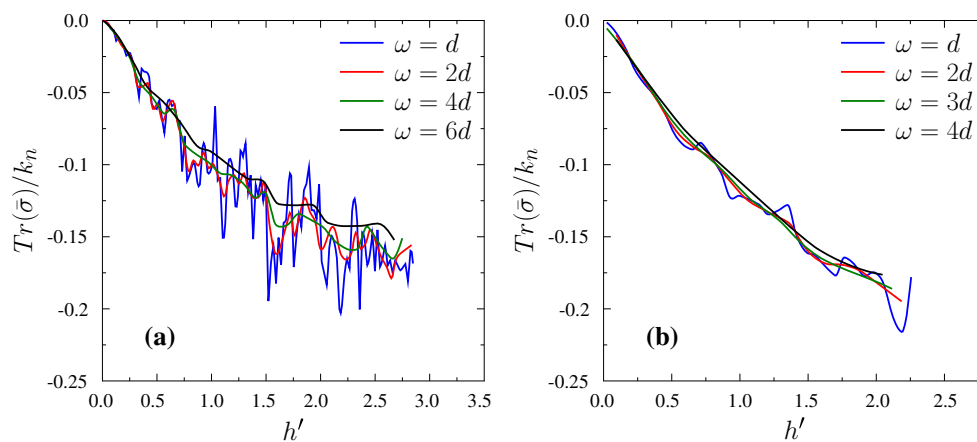
Fig. 6 Profiles of the trace of the mean stress tensor, defined by Eq. 2, after silo loading with **a** squares using an initial volume fraction $\phi_0 = 0.025$ and **b** rods of $d = 3$ with $\phi_0 = 0.04$. The depth of the silo (h) has been normalized with the width of the deposit $h' = h/W$. The results have been calculated using a Gaussian coarse-grained function, $\Phi(\mathbf{r}) = \frac{1}{\pi\omega^2} e^{-(r/\omega)^2}$, and several values of w as displayed in legends
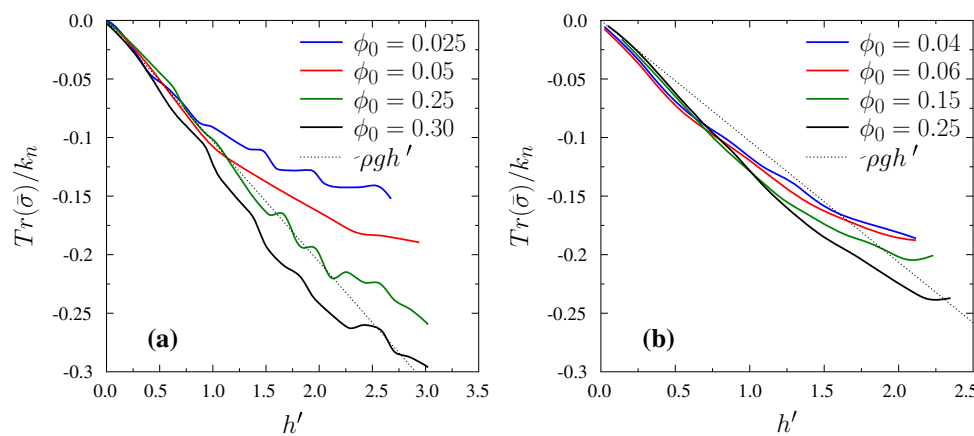

Fig. 7 Profiles of the trace of the mean stress tensor, defined by Eq. 2. The depth of the silo (h) has been normalized with the width of the deposit $h' = h/W$. The results have been calculated using a Gaussian coarse-grained function, $\phi(r) = \frac{1}{\pi\omega^2} e^{-(r/\omega)^2}$. In **a** we illustrate results for squares using $\omega = 4d$, and in **b** outcomes for rods ($d = 3$) using $\omega = 3d$ are shown. In each case, data values for several feed rates are shown. For comparison, the corresponding overburding pressure assuming $\phi = 1.0$ are also drawn

$d = 3$ (Fig. 6b) good convergence is already reached with $\omega = 3d$.

In Fig. 7 we illustrate the pressure profiles for deposits of squares and $d = 3$ rods obtained with different initial volume fractions. The pressure values have been estimated with the trace of the mean stress tensor using the corresponding optimal value for ω. In Fig. 7a deposits of squares built with different feeding rates are shown. For very low feeding rates, the high degree of order and the alignment of particles in rows along the $\phi = \pi/4$ direction lead to stress transmission towards the walls [48] and give rise to a stress profile that quickly saturates, as predicted by Janssen's mechanism [55]. When increasing the initial volume fraction, however, the stress profiles come closer to the overburden pressure (i.e., the stress produced by the weight of the granular material),

with a linear increase according to silo depth. This behavior correlates with the preferential up–down stress transmission, caused by the increase of horizontally aligned squares and enhancement of the disorder within the deposit [48]. Elongated particles, i.e. $d = 3$ rods, display similar behavior, since increasing their feeding rate also hinders pressure saturation (Fig. 7b). In this case, however, the preferred orientation is always horizontal, independently of the initial volume fraction ϕ_0. Consequently, up-down stress transmission is always favored and the changes in the stress profile are less noticeable.

Finally, it is remarkable that for both kind of particles, pressure values higher than those corresponding to the overburden profile (dotted line in Fig. 7) may be obtained. This effect is particularly marked for the highest feeding rates, for

which particle interactions become important and the time that particles take to cool down is reduced. The velocities at which particles impact the deposit are rather large; hence, it seems plausible that they get stuck in metastable configurations with strong over-stresses. These over-stresses are, then, responsible for the unexpectedly high values of pressure obtained in Fig. 7, and they agree with the negative wall pressures recently reported in *en masse*-filled 3D silos [50]. In *en masse* filling, all the particles are simultaneously generated inside the silo at the beginning of the simulations, and then they are allowed to fall by gravity until equilibrium is reached. It is reported that in *en masse* filling the wall friction on the particles may develop unrealistic contact forces, yielding pressure predictions that deviate from those expected.

5 Conclusions

We have combined experimental and numerical analysis to explore the effect that the elongation of faceted particles has on their orientation, morphology, and pressure transmission within a silo. We have also studied the role of rate of filling, in conditions ranging from very low feed rates to *en masse* filling. Elongated particles usually reveal a strong tendency to orient horizontally. This tendency is reduced as the elongation lessens. However, square particles tend to orient mainly with the diagonal parallel to the gravity. This distinctive behavior causes important differences in the pressure profiles depending on the aspect ratio of the particles.

For very low feeding rates, the packing-structure of square particles leads to stress transmission towards the walls that implies a quick development of pressure saturation. When the feed rate is increased, both the disorder and the number of horizontal squares in the silo increase, hindering the Janssen effect. For elongated particles, however, the feed rate has a weaker effect on the final deposit properties. In this case, increasing the feeding rate induces a larger fraction of horizontally aligned particles, which slightly enhances of the stress transmission in the vertical direction. We also noted pressure values above those corresponding to the overburden pressure. This behavior might be attributed to a sudden arrest of the particles that drives the deposits to metastable configurations where the grains are over-stressed. Nevertheless, further investigation is required to understand the effect of wall friction on the bulk distribution of stress in silos.

The main limitation of our analysis is the extrapolation of our results to real silos. Studying small-scale bi-dimensional silos has allowed us to explore the effect of particle shape and feeding rates on stress profile and particle arrangement. However, there is still a gap to reach the real scale of industrial silos that involve several millions of particles. Very recently, using

a DEM algorithm on general-purpose Graphics Processing Units (GPUs) has become an attractive alternative to simulate large-scale granular systems [56–59].

References

1. Matuttis, H.G.: Simulation of the pressure distribution under a two-dimensional heap of polygonal particles. Granular Matter. **1**, 83 (1998)
2. Matuttis, H.G., Luding, S., Herrmann, H.J.: Discrete element simulations of dense packings and heaps made of spherical and non-spherical particles. Powder Technol. **109**, 278292 (2000)
3. Zuriguel, I., Mullin, T., Rotter, J.M.: The effect of particle shape on the stress dip under a sandpile. Phys. Rev. Lett. **98**, 028001 (2007)
4. Zuriguel, I., Mullin, T.: The role of particle shape on the stress distribution in a sandpile. Proc. Roy. Soc. A. **464**, 99 (2008)
5. Roul, P., Schinner, A., Kassner, K.: Discrete-element computation of averaged tensorial fields in sand piles consisting of polygonal particles. Geotech. Geol. Eng. **29**, 597 (2011)
6. Hidalgo, R.C., Zuriguel, I., Maza, D., Pagonabarraga, I.: Role of particle shape on the stress propagation in granular packings. Phys. Rev. Lett. **103**, 118001 (2009)
7. Hidalgo, R.C., Zuriguel, I., Maza, D., Pagonabarraga, I.: Granular packings of elongated faceted particles deposited under gravity. J. Stat. Mech. **2010**, 06025 (2010)
8. González-Montellano, C., Ayuga, F., Ooi, J.: Discrete element modelling of grain flow in a planar silo: influence of simulation parameters. Granular Matter. **13**, 149 (2011)
9. González-Montellano, C., Ramírez, A., Gallego, E., Ayuga, F.: Validation and experimental calibration of 3D discrete element models for the simulation of the discharge flow in silos. Chem. Eng. Sci. **66**, 5116 (2011)
10. Kanzaki, T., Acevedo, M., Zuriguel, I., Pagonabarraga, I., Maza, D., Hidalgo, R.C.: Stress distribution of faceted particles in a silo after its partial discharge. Eur. Phys. J. E. **34**, 133 (2011)
11. Höhner, D., Wirtz, S., Scherer, V.: Experimental and numerical investigation on the influence of particle shape and shape approximation on hopper discharge using the discrete element method. Powder Technol. **235**, 614 (2013)
12. Azéma, E., Radjai, F., Saussine, G.: Quasistatic rheology, force transmission and fabric properties of a packing of irregular polyhedral particles. Mech. Mater. **41**, 729 (2009)
13. Börzsönyi, T., Szabó, B., Törös, G., Wegner, S., Török, J., Somfai, E., Bien, T., Stannarius, R.: Orientational order and alignment of elongated particles induced by shear. Phys. Rev. Lett. **108**, 228302 (2012)
14. Börzsönyi, T., Stannarius, R.: Granular materials composed of shape-anisotropic grains, Soft Matter. (2013) http://dx.doi.org/10.1039/C3SM50298H
15. Wegner, S., Borzsonyi, T., Bien, T., Rose, G., Stannarius, R.: Alignment and dynamics of elongated cylinders under shear. Soft Matter. **42**, 10950 (2012)
16. Nouguier-Lehon, C., Cambou, B., Vincens, E.: Influence of particle shape and angularity on the behavior of granular materials: a numerical analysis. Int. J. Numer. Anal. Meth. Geomech. **27**, 1207 (2003)

17. Fukumoto, Y., Sakaguchi, H., Murakami, A.: The role of rolling friction in granular packing. Granular Matter. **15**, 175 (2013)
18. Iwashita, K., Oda, M.: Rolling resistance at contacts in simulation of shear band development by DEM. Powder Technol. **109**, 192 (2000)
19. Kloss, C., Goniva, C., Hager, A., Amberger, S., Pirker, S.: Models, algorithms and validation for opensource DEM and CFD–DEM. Prog. Comput. Fluid Dyn. Int. J. **12**, 140 (2012)
20. Cundall, P.A., Strack, O.D.L.: A discrete numerical model for granular assemblies. Géotechnique **29**, 47 (1979)
21. Latham, J.-P., Munjiza, A., Garcia, X., Xiang, J., Guises, R.: Three-dimensional particle shape acquisition and use of shape library for DEM and FEM/DEM simulation. Miner. Eng. **21**, 797 (2008)
22. Williams, J., Pentland, A.: Super-quadrics and modal dynamics for discrete elements in interactive design. Eng. Comput. Int. J. Comput. Aided Eng. **9**, 115 (1992)
23. Tillemans, H.J., Herrmann, H.J.: Simulating deformations of granular solids under shear. Phys. A **217**, 261 (1995)
24. Kun, F., Herrmann, H.J.: Transition from damage to fragmentation in collision of solids. Phys. Rev. E. **59**, 2623 (1999)
25. Azéma, E., Radjai, F., Dubois, F.: Packings of irregular polyhedral particles: Strength, structure, and effects of angularity. Phys. Rev. E **87**, 062203 (2013)
26. Azéma, E., Radjai, F., Saint-Cyr, B., Delenne, J.Y., Sornay, P.: Rheology of three-dimensional packings of aggregates: microstructure and effects of nonconvexity. Phys. Rev. E **87**, 052205 (2013)
27. Boton, M., Azéma, E., Estrada, N., Radjai, F., Lizcano, A.: Quasi-static rheology and microstructural description of sheared granular materials composed of platy particles. Phys. Rev. E **87**, 032206 (2013)
28. Höhner, D., Wirtz, S., Kruggel-Emden, H., Scherer, V.: Comparison of the multi-sphere and polyhedral approach to simulate non-spherical particles within the discrete element method: Influence on temporal force evolution for multiple contacts. Powder Technol. **208**, 643 (2011)
29. Höhner, D., Wirtz, S., Scherer, V.: A numerical study on the influence of particle shape on hopper discharge within the polyhedral and multi-sphere discrete element method. Powder Technol. **226**, 16 (2012)
30. Pournin, L., Liebling, T.M.: From spheres to spheropolyhedra: generalized distinct element methodology and algorithm analysis. In: Cook, W., Lovász, L., Vygen, J. (eds.) Res. Trends Comb. optim., pp. 347–363. Springer, Berlin (2009)
31. Alonso-Marroquin, F.: Spheropolygons: a new method to simulate conservative and dissipative interactions between 2D complex-shaped rigid bodies. Europhys. Lett. **83**, 14001 (2009)
32. Galindo-Torres, S.A., Alonso-Marroquin, F., Wang, Y.C., Pedroso, D., Munoz-Castano, J.D.: Molecular dynamics simulation of complex particles in 3D and the study of friction due to non-convexity. Phys. Rev. E. **79**, 060301 (2009)
33. Alonso-Marroquin, F., Ramirez-Gomez, A., Gonzalez-Montellano, C., Balaam, N., Hanaor, D.A.H., Flores-Johnson, E.A., Gan, Y., Chen, S., Shen, L.: Experimental and numerical determination of mechanical properties of polygonal wood particles and their flow analysis in silos. Granular Matter. **15**, 811 (2013)
34. Gethin, D.T., Yang, X.S., Lewis, R.W.: A two dimensional combined discrete and finite element scheme for simulating the flow and compaction of systems comprising irregular particulates. Comput. Methods Appl. Mech. Eng. **195**, 5552 (2006)
35. Munjiza, A.: The Combined Finite-Discrete Element Method. Wiley, New York (2004)
36. Guises, R., Xiang, J., Latham, J.-P., Munjiza, A.: Granular packing: numerical simulation and the characterization of the effect of particle shape. Granular Matter. **11**, 281 (2009)
37. Lätzel, M., Luding, S., Herrmann, H.J.: Macroscopic material properties from quasi-static, microscopic simulations of a two-dimensional shear-cell. Granular Matter. **2**, 123 (2000)
38. Madadi, M., Tsoungui, O., Lätzel, M., Luding, S.: On the fabric tensor of polydisperse granular media in 2D. Int. J. Solids Struct. **41**, 2563 (2004)
39. Glasser, B.J., Goldhirsch, I.: Scale dependence, correlations, and fluctuations of stresses in rapid granular flows. Phys. Fluids **13**, 407 (2001)
40. Goldhirsch, I., Goldenberg, C.: On the microscopic foundations of elasticity. Eur. Phys. J. E **9**, 245251 (2002)
41. Goldhirsch, I.: Stress, stress asymmetry and couple stress: from discrete particles to continuous fields. Granular Matter. **12**, 239 (2010)
42. Weinhart, T., Thornton, A.R., Luding, S., Bokhove, O.: From discrete particles to continuum fields near a boundary. Granular Matter. **14**, 289 (2012)
43. Weinhart, T., Hartkamp, R., Thornton, A.R., Luding, S.: Coarse-grained local and objective continuum description of 3D granular flows down an inclined surface. Phys. Fluids **6**, 25 (2013)
44. Luding, S., Lätzel, M., Herrmann, H.J.: From discrete element simulations towards a continuum description of particulate solids. In: Levy, A., Kalman, H. (eds.) Handbook of Conveying and Handling of Particulate Solids, pp. 39–44. Elsevier, Amsterdam (2001)
45. Ai, J., Chen, J.-F., Ooi, J.Y.: Finite element simulation of the pressure dip in sandpiles. Int. J. Solids Struct. (in press). http://dx.doi.org/10.1016/j.ijsolstr.2012.12.006
46. Geng, J., Longhi, E., Behringer, R.P., Howell, D.W.: Memory in two-dimensional heap experiments. Phys. Rev. E **64**, 060301(R) (2001)
47. Zhong, Z., Ooi, J.Y., Rotter, J.M.: The sensitivity of silo flow and wall stresses to filling method. Eng. Struct. **23**, 756 (2001)
48. Acevedo, M., Hidalgo, R.C., Zuriguel, I., Maza, D.: Influence of the feeding mechanism on deposits of square particles. Phys. Rev. E. **87**, 012202 (2013)
49. Hidalgo, R.C., Acevedo, M., Zuriguel, I., Pagonabarraga, I., Maza, D.: Influence of the feeding rate on the packing properties of faceted particles. AIP Conf. Proc. **1542**, 895–898 (2013)
50. González-Montellano, C., Ramírez, A., Fuentes, J.M., Ayuga, F.: Numerical effects derived from en masse filling of agricultural silos in DEM simulations. Comput. Electron. Agric. **81**, 113 (2012)
51. Bartos, I., Janosi, I.M.: Side pressure anomalies in 2D packings of frictionless spheres. Granular Matter. **9**, 81 (2007)
52. Sibille, L., Mullin, T., Poullain, P.: The effect of particle shape on the marginal rigidity state in 2D granular media. Europhys Lett. **86**, 44003 (2009)
53. Pugnaloni, L.A., Sánchez, I., Gago, P.A., Damas, J., Zuriguel, I., Maza, D.: Towards a relevant set of state variables to describe static granular packings. Phys. Rev. E. **82**, 050301(R) (2010)
54. Carlevaro, C.M., Pugnaloni, L.A.: Steady state of tapped granular polygons. J. Stat. Mech. **2011**, 01007 (2011)
55. Janssen, H.A., Zeitschr, d: Versuche über Getreidedruck in Silozellen. Vereines deutscher Ingenieure **39**, 1045 (1895)
56. Owens, J., Luebke, D., Govindaraju, N., Harris, M., Krüger, J., Lefohn, A., Purcell, T.: A survey of general-purpose computation on graphics hardware. Comput. Graph. Forum. **26**, 80 (2007)
57. Owens, J., Houston, M., Luebke, D., Green, S., Stone, J., Phillips, J.: GPU computing. Proc. IEEE. **96**, 879 (2008)
58. Longmore, J.-P., Marais, P., Kuttel, M.: Towards realistic and inter-active sand simulation: a GPU-based framework. Powder Technol. **235**, 983 (2013)
59. Hidalgo, R.C., Kanzaki, T., Alonso-Marroquin, F., Luding, S.: On the use of graphics processing units (GPUs) for molecular dynamics simulation of spherical particles. AIP. Conference Proceedings 1542, p 169 (2013)